Atmospheric
Chemistry
and Physics

Supplement of

Observations of high-time-resolution and size-resolved aerosol chemical composition and microphysics in the central Arctic: implications for climate-relevant particle properties

Benjamin Heutte et al.

Correspondence to: Julia Schmale (julia.schmale@epfl.ch)

S1 Information on the high-resolution time-of-flight aerosol mass spectrometer (AMS) dataset

S1.1 Detection limits of the AMS

The detection limits for the five non-refractory chemical species measured with the AMS (i.e., sulfate, nitrate, ammonium, chloride, and organics) were computed using Eq. S1 (Drewnick et al., 2009):

$$DL_n = \frac{3 * SD}{\sqrt{\dfrac{n}{m}}} \tag{S1}$$

Where DL_n is the detection limit at a time resolution of n min, SD is the standard deviation of the species' mass concentrations during filter period measurements, n is the averaged time resolution, and m is the output time resolution of the instrument (i.e., 60 sec during MOCCHA and 90 sec during MOSAiC). The calculations were done separately for the four different periods discussed in the manuscript (i.e., Aug-Sep, Oct-Dec, Mar-May, and Jun-Jul). Detection limits for all measured species, at the averaged time resolutions of 10 min and 1 h, are given in Table S1, along with the percentage of unpolluted data below the detection limit at 1 h time resolution for each period.

Table S1: Detection limits (DL) for the five main non-refractory species during the different analysis periods, at 10 min / 1 h time resolutions. The percentage of unpolluted data below the detection limit at 1 h time resolution is given in parenthesis for each period. The detection limits were calculated as three times the standard deviation of each species' mass concentration during filter period measurements divided by the square root of the averaging time (Eq. S1). Values are given in units of ng/m³.

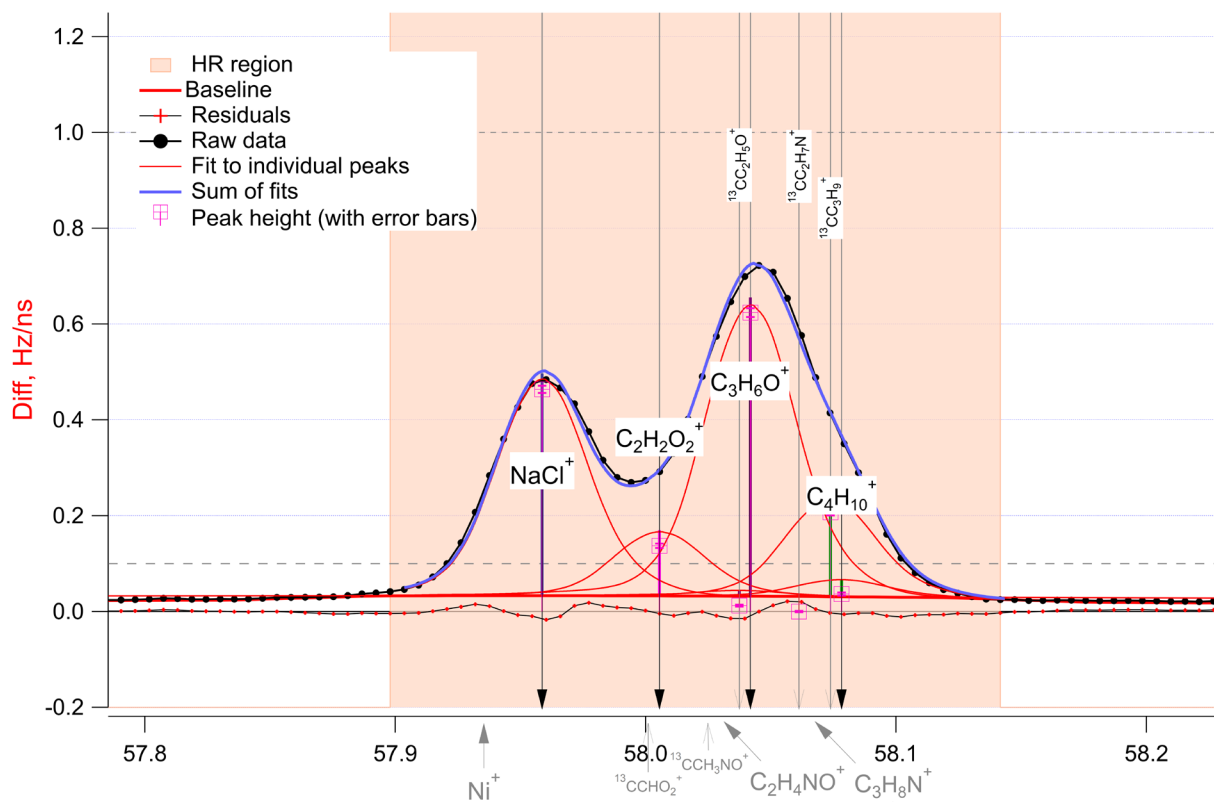|	MOCCHA: Aug-Sep	MOSAiC: Oct-Dec	MOSAiC: Mar-May	MOSAiC: Jun-Jul
Sulfate	10 / 4 (19 %)	23 / 9 (5 %)	24 / 10 (1 %)	11 / 5 (13 %)
Nitrate	13 / 5 (25 %)	14 / 6 (1 %)	17 / 7 (0.1 %)	20 / 8 (83 %)
Ammonium	1 / 0.4 (99 %)	2 / 1 (83 %)	5 / 2 (1 %)	-
Chloride	7 / 3 (98 %)	27 / 11 (2 %)	14 / 6 (1 %)	10 / 4 (37 %)
Organics	110 / 45 (42 %)	80 / 33 (17 %)	62 / 25 (2 %)	138 / 56 (9 %)

S1.2 Sea salt detection with the AMS

Figure S1: NaCl$^+$ peak fitting procedure at *mz* 58. The peak fitting was done using the Peak Integration by Key Analysis (PIKA) v1.25B within the IGOR Pro v9.00 software. The data shown here are of the *difference* signal, which is the difference between the open and closed signal.
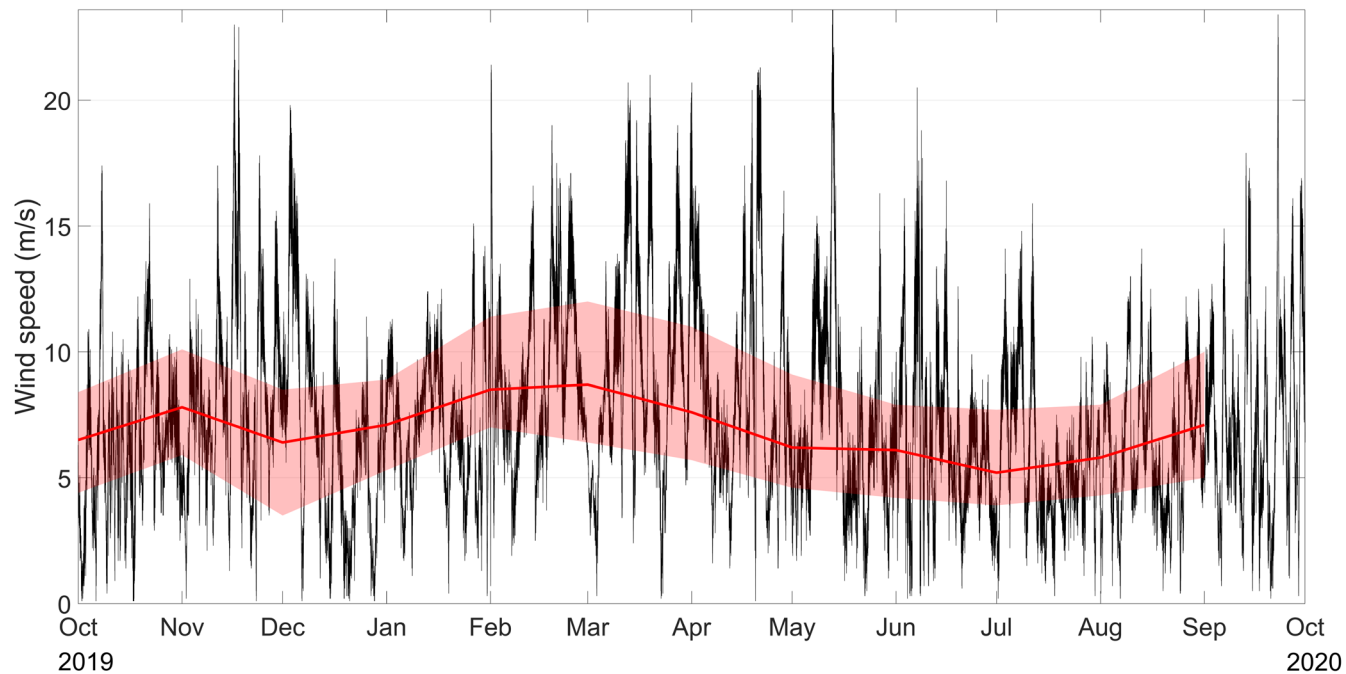
50

55

60

S2 Wind speed seasonality

Figure S2: Wind speed annual cycle during MOSAiC. The black lines represent the 1 min wind speed measured onboard Polarstern, while the thick red line correspond to the monthly medians. The shaded red region shows the interquartile range.

65

70

75

4

S3 High-resolution case studies from November 2019 and March 2020

80   **S3.1 Strom case study from March 2020**

We have seen in Sect. 3.2 how, under synoptic scale meteorological events, local and remote sources of aerosols can elevate aerosol mass and number concentrations from the low background values in autumn, having climate-relevant implications for the central Arctic cloud formation and radiative budget. The question arises whether these storm-induced high-concentration events were also observed in spring when the background particle concentration was much higher (haze), and if so, whether

85   the implications are comparable to autumn. We present in Fig. S3 two spring storms in March 2020, where the same variables as in Fig. 5 are discussed.

S3.1.1 Wind-dependent aerosol generation as a local source of aerosols

On March 15th, the wind speed increased rapidly reaching a maximum of 17 m/s. Blowing or drifting snow was detected from 7:00 on the 15th to 10:00 on the 17th. Similarly to the storms presented in Sect. 3.2, the increasing wind speed was associated

90   with increases in aerosol properties, where $N_{>1000nm}$ increased by a factor of ~3 (from 7.0 cm^{-3} before the storm, from 13:00 on the 14th to 6:00 on the 15th, to 21.6 cm^{-3} at the highest, from 7:00 to 9:00 on the 15th) and the NaCl signal increased by a factor of ~4 (from 0.03 to 0.12 a.u.). Here as well, the NaCl and $N_{>1000nm}$ signals were highly correlated during the blowing snow period ($\rho_{pearson} = 0.83$, p-value < 0.001). Simultaneously, CCN number concentrations were increased by a factor of ~2 at all SS levels compared to background (from 121.7 to 229.9 cm^{-3} at 0.15% SS, from 177.6 to 313.1 cm^{-3} at 0.3% SS, and from

95   254.4 to 417.3 cm^{-3} at 1% SS). It however appears that the CCN number concentrations were already quite high before the storm, especially at 1% SS, as the result of an important contribution of Aitken mode particles at that time (see Fig. S5a). The correlation between CCN number concentrations and the NaCl signal was also lower at 1% SS ($\rho_{pearson} = 0.66$, p-value < 0.001) than at 0.15% SS ($\rho_{pearson} = 0.82$, p-value < 0.001). This indicates that the Aitken mode particle population (relevant for SS = 1%) is different from the one in fall, where CCN and NaCl correlated with $\rho_{pearson} = 0.88$. Given that an Aitken mode was

100   already present prior to the storm, there were likely at least two particle populations within this size range. The scattering coefficient increased by a factor of ~3 (from 16.6 to 46.2 Mm^{-1}) during the storm and correlated greatly with the NaCl signal ($\rho_{pearson} = 0.85$, p-value < 0.001). Finally, eBC mass concentrations seemed to follow the NaCl signal, with a storm-peak increase by a factor of ~2 (from 0.10 to 0.21 µg/m^3). However, the low eBC data availability at that time was insufficient to draw robust conclusions on the source of eBC related to the increase, whether it was locally emitted through blowing snow or

105   long-range transported. While the influence of local pollution from *Polarstern* reduced the amount of available data for the second storm from March 26th to March 29th, especially for eBC mass and CCN number concentrations, the same conclusion as for the first storm could be drawn regarding the relations between wind speed, NaCl signal, $N_{>1000nm}$, and the scattering coefficient. In particular, the peak in wind speed on the 27th (from around 7:00 to 11:00 pm), under blowing snow conditions,

Figure S3: High-time resolution case studies of two storms in March 2020 during MOSAiC. Refer to Fig. 5 for a description of the variables included in all panels. The snowdrift density was derived from the snow particle counter mounted at 8 cm above ground. All measurements were averaged to 10 min time resolution, except for CO_2 which is hourly and LF_{div} which depends on satellite data availability. $LF_{5x\ accu,\ div}$ data were not available for the first storm (panel (a)). Data identified as affected by local contamination (pollution) were removed, except for NaCl which did not exhibit any reaction to local pollution during these periods. NaCl signals are in arbitrary units.

was associated with increases in $N_{>1000nm}$ from 4.8 to 16.5 cm^{-3} (increase by a factor of ~3), in NaCl from 0.04 to 0.13 a.u. (~3), and in the scattering coefficient from 10.4 to 25.5 Mm^{-1} (~3), compared to background conditions on the 26th.

Finally, as discussed in Sect. 3.2.1, wind-generated SSA from open leads and the ice-free ocean may have also contributed to the observed increase in the variables mentioned above. The co-occurrence in the observed drifting snow, NaCl signal, and $N_{>1000nm}$, coupled with the relatively small lead fraction (< 1 % and < 2.5 % for the first and second storm, respectively), however, suggest that the influence of blowing snow may have been dominant over SSA from leads during the blowing snow periods.

6

S3.1.2 Long-range transport as a remote source of aerosols

The increase in wind speed on March 15th was associated with a rising CO_2 mixing ratio (~ 2 ppm increase), covarying with SO_4^{2-} mass concentrations ($\rho_{pearson}$ = 0.66 and p-value < 0.001 during the blowing snow period). Organics followed a similar temporal evolution. SO_4^{2-} and Org mass concentrations peaked with a six to seven hours delay compared to the peak in NaCl signal, indicating that the source of these particles was different. This is also observed in the different behavior between the PNC in the size range 10-80 nm and 80-200 nm (see Fig. S5a). The observed increases in SO_4^{2-} (from 0.51 to 0.85 µg/m³) and Org (from 0.34 to 0.78 µg/m³) mass concentrations by a factor of ~2 were associated with long-range transport of pollution from eastern Siberia (see Fig. S7a) and a strong cyclone activity (Rinke et al., 2021). The impact that these long-range transported particles had on the CCN population here is difficult to quantify given the apparent co-occurrence of locally and remotely-emitted particles during the storm. Despite the low data availability during the March 26th-29th storm, the influence of long-range transported particles seemed to be limited, with little to no variations in CO_2 mixing ratio as well as SO_4^{2-} and Org mass concentrations. While back-trajectories at that time pointed towards Siberia being a potential source region (see Fig. S7b), it appeared that the transported air masses were relatively clean compared to e.g., the March 15th storm.

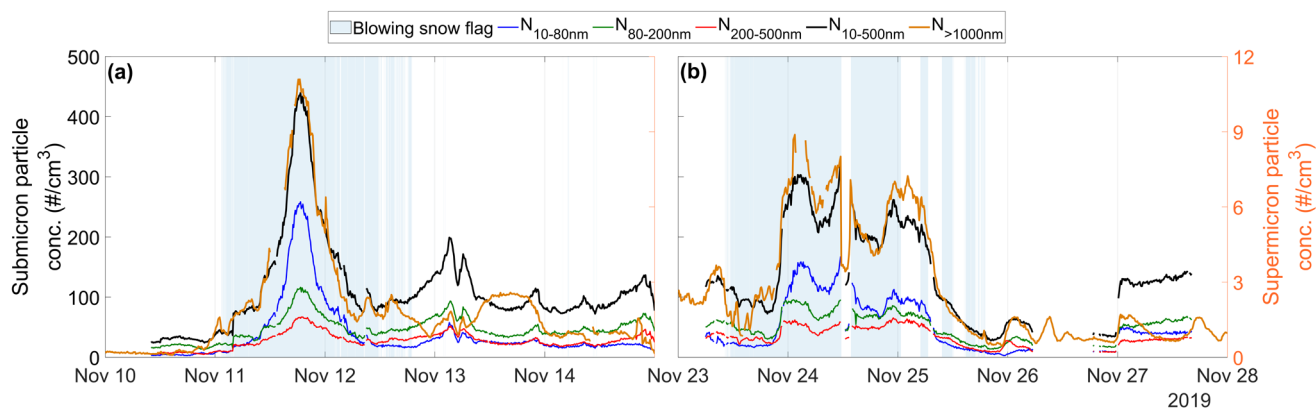### S3.2 Comparison of sub- and supermicron particle number concentrations

Figure S4: Timeseries of sub- and supermicron particle number concentrations during the (a) November 10th to 15th, 2019 and (b) November 23rd to 28th, 2019 storms. The submicron particle number concentrations were further separated in the size ranges from 10-80 nm, 80-200 nm, and 200-500 nm. For both panels, a blue shading indicates periods when blowing/drfiting snow was detected. All measurements were averaged (arithmetic mean) to 10 min time resolution. Data identified as affected by local contamination (pollution) were removed.
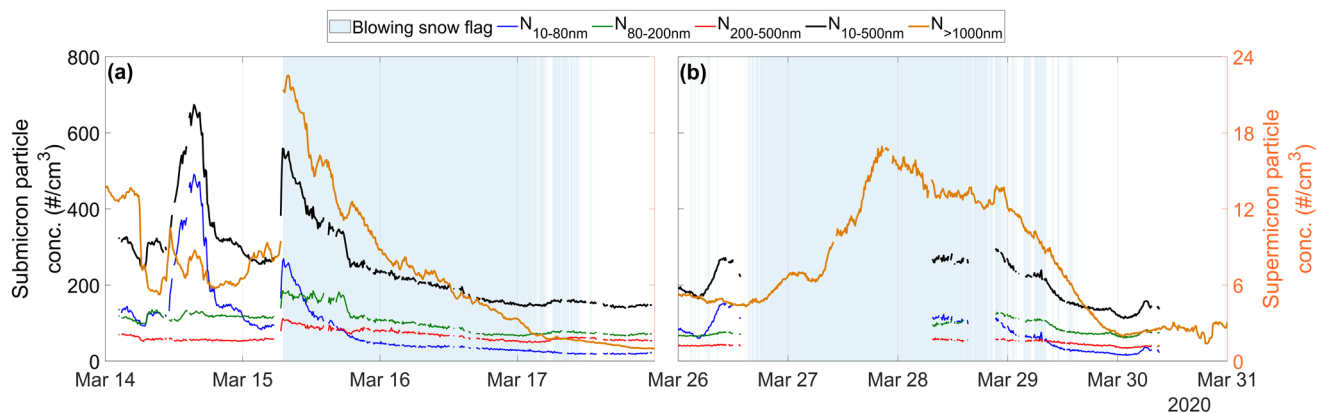
Figure S5: Timeseries of sub- and supermicron particle number concentrations during the (a) March 14th to 18th, 2020 and (b) March 26th to 31st, 2020 storms. The submicron particle number concentrations were further separated in the size ranges from 10-80 nm, 80-200 nm, and 200-500 nm. For both panels, a blue shading indicates periods when blowing snow was detected. All measurements were averaged (arithmetic mean) to 10 min time resolution. Data identified as affected by local contamination (pollution) were removed.

S3.3 Source region: FLEXPART back-trajectories

S3.3.1 Method

To identify the source regions of air masses associated with the November (Fig. 5) and March (Fig. S3) storms, we used Lagrangian backward dispersion model simulations from FLEXPART v10.4 (Pisso et al., 2019), performed by the University of Vienna. The simulations were driven by ERA5 meteorological reanalysis data, on a spatial grid with a 0.5° x 0.5° resolution. Every 3 h, along RV *Polarstern*'s track, a cluster of 100,000 particles (passive air tracer) was released and tracked backward in time for 10 days. For our analysis, we summed the residence time of all the particles in each grid cell for the duration of the storm event, when the air had been traveling in the lowest vertical layer of the simulation (i.e., below 100 m). The results of the analysis are shown in Fig. S6 for the two case studies of storms in November and in Fig. S7 for the March storms.

S3.3.2 Back-trajectories for the November 2019 and March 2020 storms
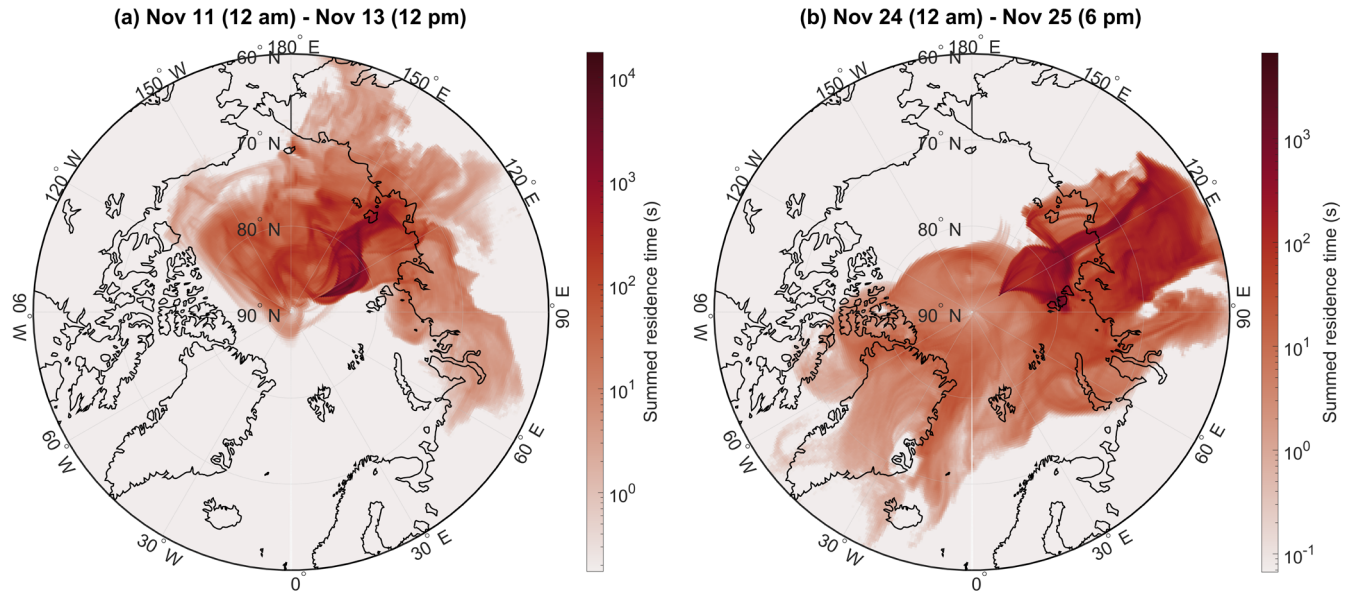

Figure S6: Air-mass back-trajectories during two storms in November 2019, from (a) Nov 11 (12:00 am UTC) to Nov 13 (12:00 pm UTC) and (b) from Nov 24 (12:00 am UTC) to Nov 25 (6:00 pm UTC). The colorscale represents the summed residence time of the particle tracers in each grid cells for the 10-days FLEXPART back-trajectories over the periods of interest.
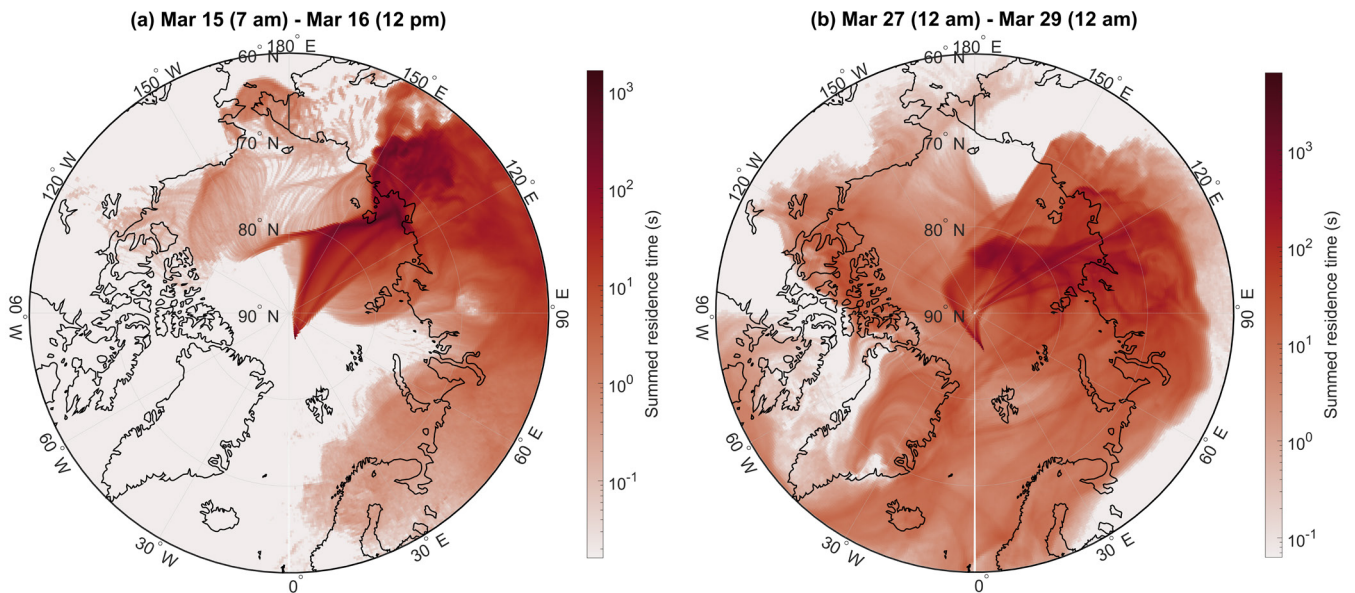

Figure S7: Air-mass back-trajectories during two storms in March 2020, from (a) Mar 15 (7:00 am UTC) to Mar 16 (12:00 pm UTC) and (b) from Mar 27 (12:00 am UTC) to Mar 29 (12:00 am UTC). The colorscale represents the summed residence time of the particle tracers in each grid cells for the 10-days FLEXPART back-trajectories over the periods of interest.

S4 Clustering of the particle number size distributions in autumn and spring

160 **S4.1 Selecting the optimal number of clusters**

The number of clusters for the solution was varied from 3 to 30. For each run, the Within-Cluster Sum of Squares (WCSS) was calculated and plotted against the number of clusters (Fig. S8b for Oct-Nov and Fig. S10b for Mar-Apr), and the optimal number of clusters was selected at the estimated inflection point (or "elbow") of the curve. Following this approach, the 8 clusters solution was employed for the October-November period (see Fig. S8a) while the 7 clusters solution was chosen for

165 the March-April period (see Fig. S10a). Adding more clusters didn't yield any significant difference but only isolated particular events with shared characteristics (e.g., two different blowing snow events).

The resulting clusters were further manually merged into 4 clusters for October-November and 3 clusters for March-April based on the similarities of the clusters' median size distribution as well as the potential sources associated with them. Starting

170 with the October-November period, the *blowing snow* (*BLSN*) cluster is solely constituted of Cluster 1 from Fig. S8a. It was named as such given the significantly larger sea salt concentrations associated with this cluster (see Table 1) and appeared to match well with the flagged periods of blowing snow (see Fig. S9) parametrized from snowdrift density and near-surface wind speed observations (Gong et al., 2023). The *long-range transport* (*LRT*) cluster is also solely constituted of Cluster 3, while the *LRT aged* cluster is composed of Clusters 6 and 7, which are characterized by fewer but larger particles. Finally, all clusters

175 with an amplitude of the main (accumulation) mode below 50 cm^{-3} (i.e., Clusters 1, 4, 5, and 8) were grouped into the *background* (*BG*) cluster. For the March-April period, clusters 3 and 7 from Fig. S10a were merged into the spring *BLSN* clusters. Occurrences of the *BLSN* cluster in March-April also matched relatively well with the parametrized blowing snow flag (see Fig. S11). The *haze bimodal* cluster groups all of the original clusters with bimodal median number size distributions (i.e., Clusters 1, 4, and 6). Finally, the very similar Clusters 2 and 5, characterized by monomodal number size distributions

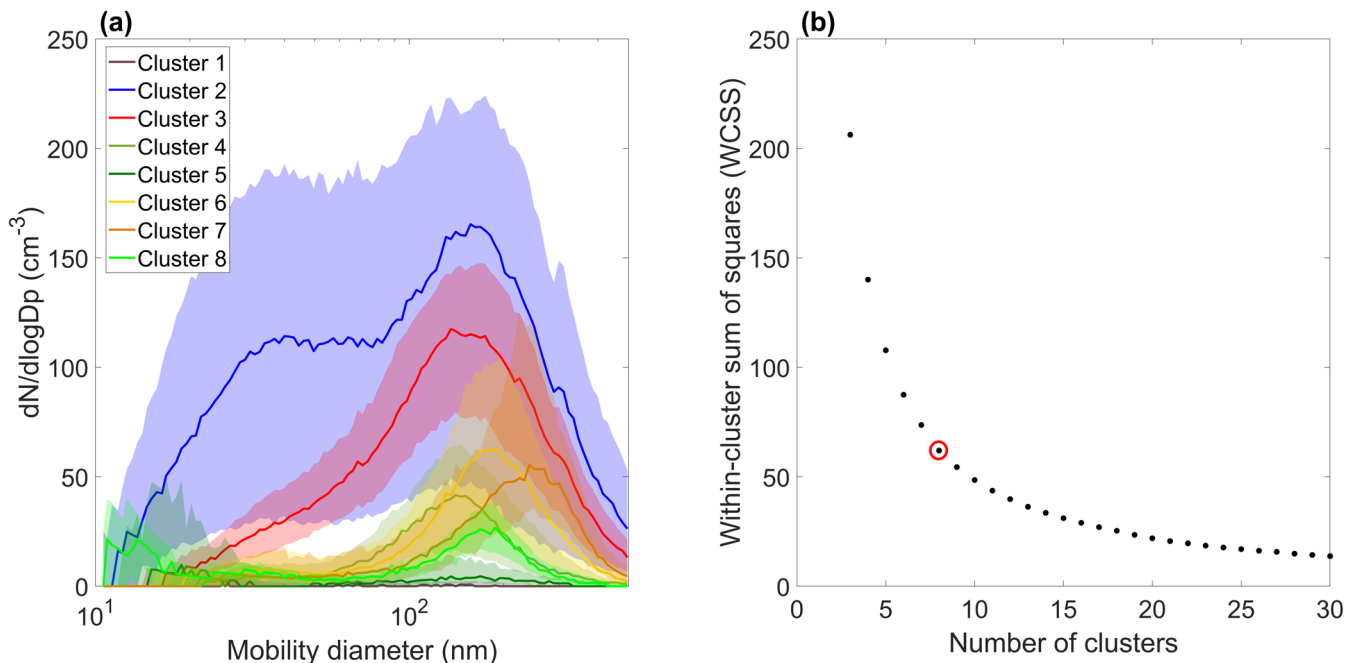180 and a strong contribution of accumulation mode particles, were grouped into the *haze* cluster.

Figure S8: Distributions of the eight PNSD clusters for the October-November period. The median (thick colored lines) and interquartile range (transparent colored envelops) of the eight PNSD clusters are shown in (a). Panel (b) shows the "elbow curve" of the within-cluster sum of squares (WCSS) as a function of the number of clusters, varied from 3 to 30. The red circle outlines the chosen solution (i.e., 8 clusters) at the estimated inflection point of the curve.
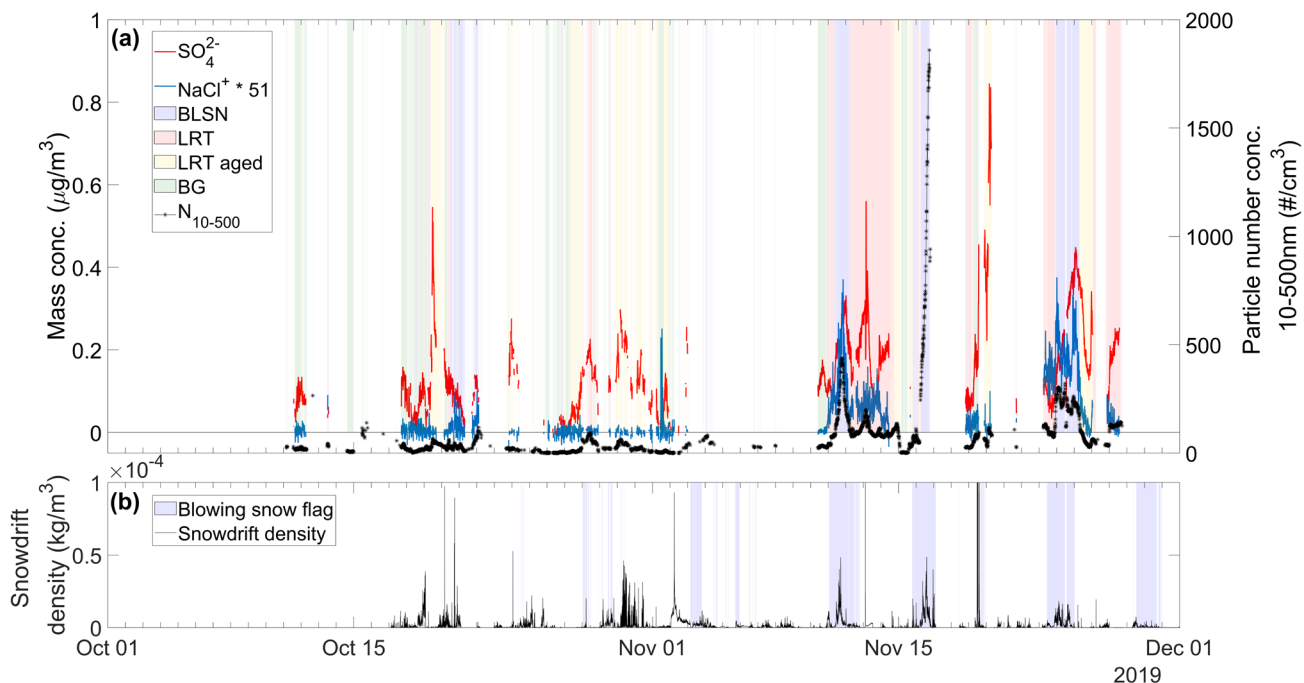

Figure S9: Temporal evolution of the merged PNSD clusters and comparison with the parametrized blowing snow flag for the Oct-Nov 2019 period. For sulfate (SO_4^{2-}) and sea salt (NaCl) only the timesteps where data were available with the SMPS were kept. NaCl mass concentrations are in arbitrary units.
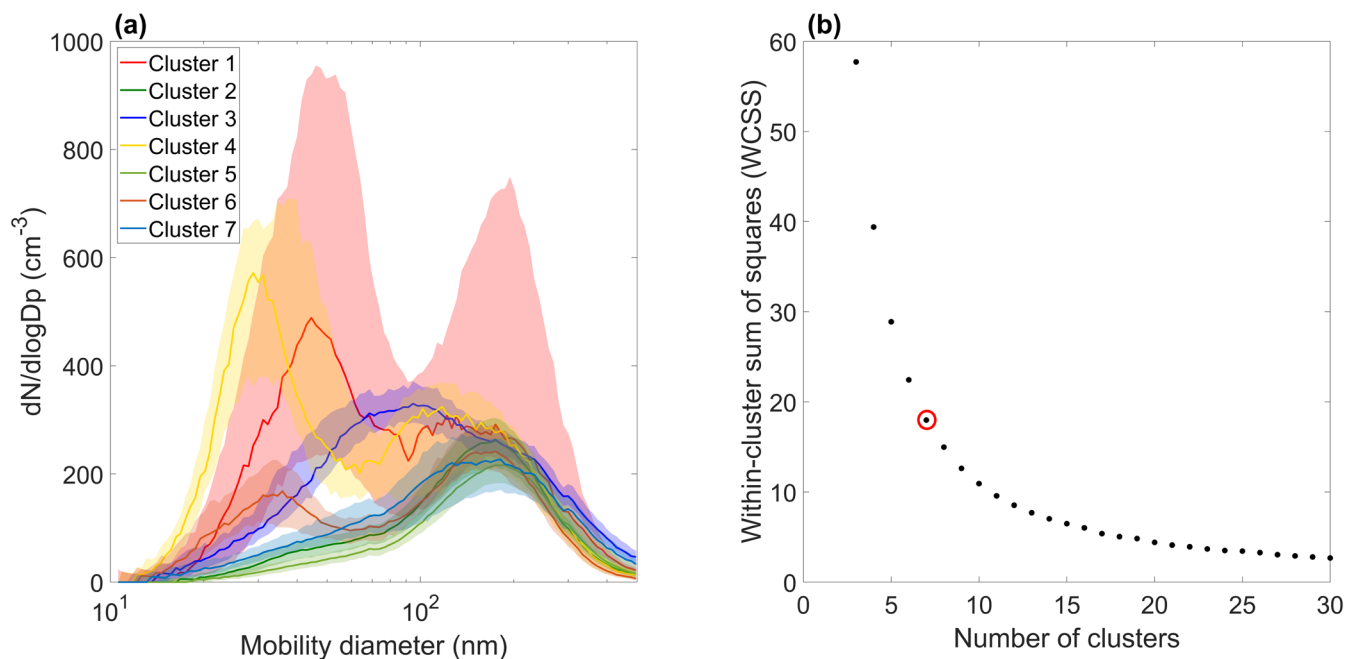
Figure S10: Distributions of the eight PNSD clusters for the March-April period. The median (thick colored lines) and interquartile range (transparent colored envelops) of the eight PNSD clusters are shown in (a). Panel (b) shows the "elbow curve" of the within-cluster sum of squares (WCSS) as a function of the number of clusters, varied from 3 to 30. The red circle outlines the chosen solution (i.e., 7 clusters) at the estimated inflection point of the curve.
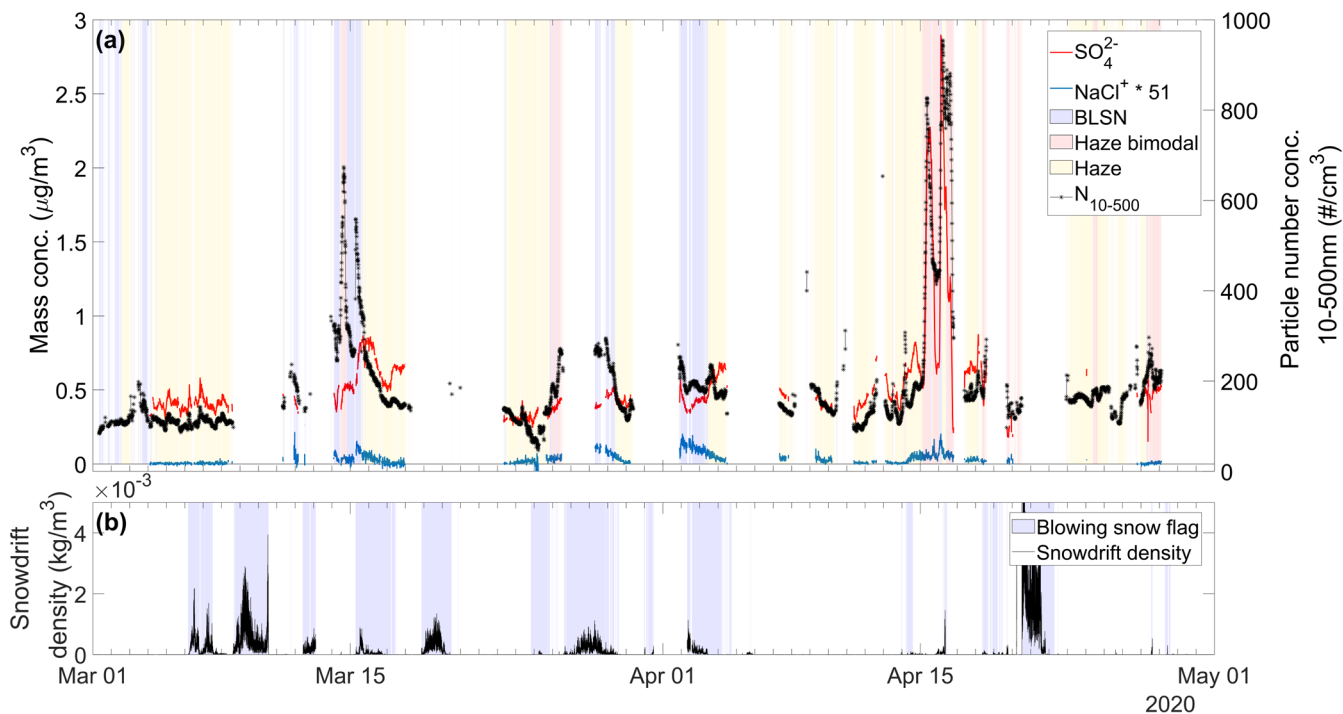

Figure S11: Temporal evolution of the merged PNSD clusters and comparison with the parametrized blowing snow flag for the Mar-Apr 2020 period. For sulfate (SO_4^{2-}) and sea salt (NaCl) only the timesteps where data were available with the SMPS were kept. NaCl mass concentrations are in arbitrary units.
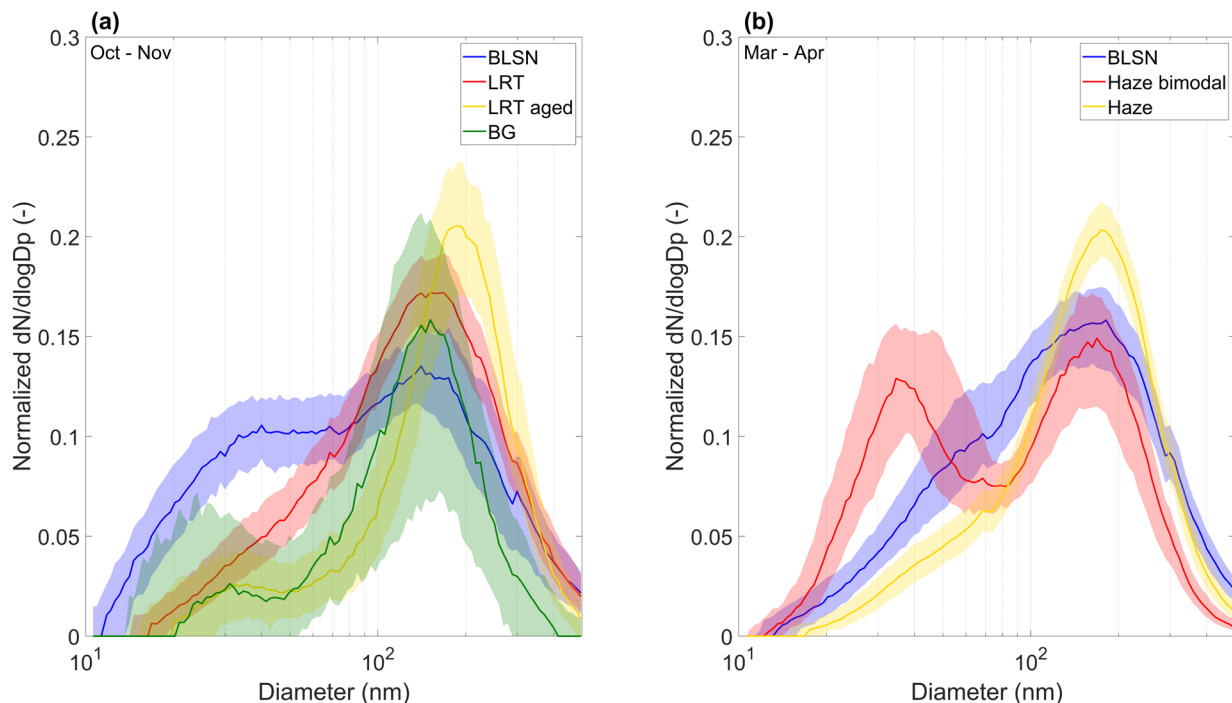
Figure S12: Clustered PNSD in (a) October-November and (b) March-April. This is the same figure as Fig. 6, except that here the number size distributions are normalized to the vector length to compare the shapes of the PNSDs.

S4.2 Modal parameters of the cluster's fitted distributions

Table S2: Fitting modal parameters (location of mode and amplitude) for the bimodal log-normal distributions fitted on the median PNSDs of the clusters in Oct-Nov (autumn) and Mar-Apr (spring). The fitting was done using the "Multipeak fitting" package within IGOR Pro v9.02. Errors represent the fitting error and are not a measure of the statistical variance.

	Mode 1		Mode 2	
	Location (nm)	**Amplitude (cm^{-3})**	**Location (nm)**	**Amplitude (cm^{-3})**
BLSN (autumn)	36 ± 1	108.4 ± 1.1	165 ± 2	156.2 ± 1.1
LRT (autumn)	41 ± 1	24.9 ± 0.6	155 ± 1	115.6 ± 0.4
LRT aged (autumn)	44 ± 1	6.9 ± 0.2	192 ± 1	55.4 ± 0.3
BG (autumn)	38 ± 2	3.4 ± 0.2	148 ± 1	16.9 ± 0.2
BLSN (spring)	43 ± 2	70.4 ± 4.2	156 ± 3	245.3 ± 2.9
Haze bimodal (spring)	38 ± 0.2	227.0 ± 1.6	163 ± 1	253.7 ± 1.7
Haze (spring)	57 ± 1	52.0 ± 0.6	176 ± 1	229.3 ± 1.0

190   **S5 Size-resolved chemical composition**

Table S3: Mode location (in vacuum aerodynamic diameter) for the monthly averaged (median) sulfate and organics mass size distributions. The mode diameters were retrieved by fitting a monomodal log-normal distribution to each monthly mass size distribution. Errors represent the fitting error and are not a measure of the statistical variance.

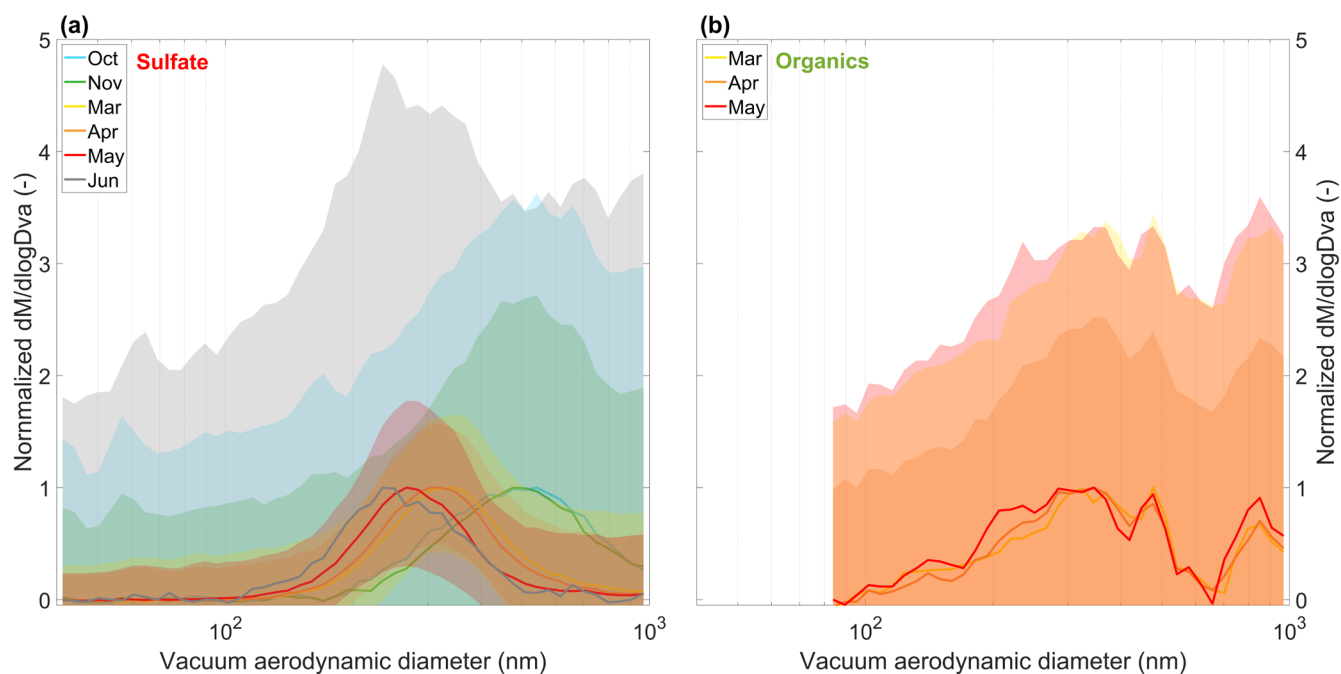|	**Sulfate's mode location (nm)**	**Organics' modes location (nm)**
October	486 ± 3	-
November	494 ± 2	-
March	332 ± 2	338 ± 8
April	315 ± 1	325 ± 5
May	277 ± 1	299 ± 8
June	257 ± 2	-

Figure S13: Species-specific size distributions of sulfate (a) and organics (b) during MOSAiC, presented as monthly median values. The thick colored lines represent the medians of the species-specific size distributions, which were normalized by the distributions' maximum value. Shaded regions represent the interquartile range (25th – 75th quantiles) of the distributions, which were also normalized to the maximum of the 50th quantile (median) of the distributions. All the months that are not shown in both panels had a signal-to-noise ratio too low for the PToF data to be analyzed, mainly for organics outside of the spring months. The monthly medians exclude polluted data for both sulfate and organics. Due to gas-phase interactions with the organics' PToF signal, the size distributions of organics in (b) were truncated below 80 nm.
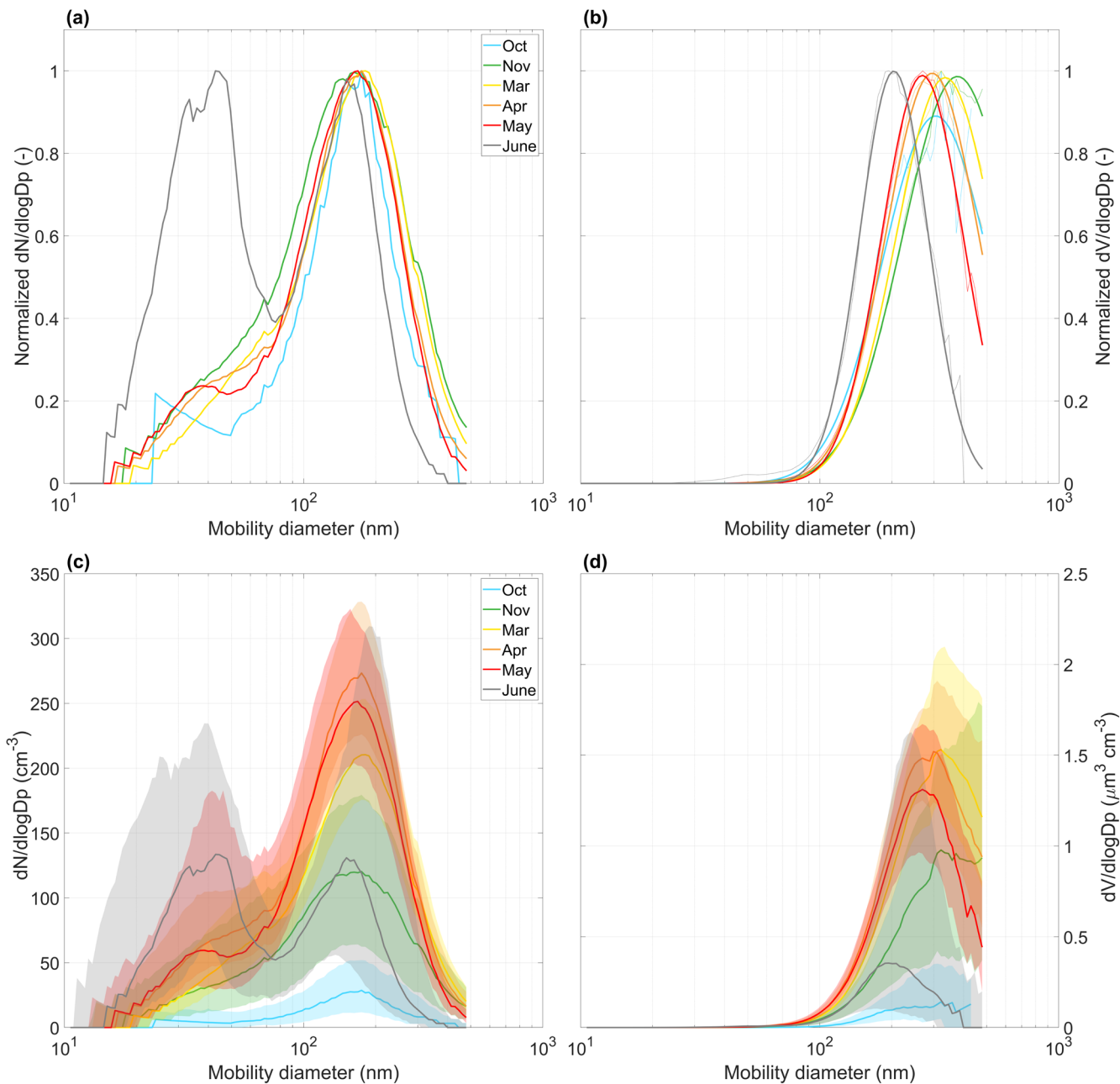
195

14

Figure S14: Particle number (a, c) and volume (b, d) size distributions for October, November, March, April, May, and June, during MOSAiC based on SMPS measurements. In panel (a) and (b), the monthly medians were normalized by the distributions' maximum value to compare their shape. The particle volume size distributions in (b) were fitted with monomodal log-normal distributions and resulting mode diameters were found at 305 ± 5, 376 ± 2, 334 ± 1, 295 ± 1, 268 ± 1, and 204 ± 1 nm for Oct, Nov, Mar, Apr, May, and Jun, respectively. In panel (c) and (d), the monthly medians are given as absolute values, where the shaded region represents the interquartile range. Data identified as affected by local contamination were not considered in the computation of the monthly statistics.

References

Drewnick, F., Hings, S. S., Alfarra, M. R., Prevot, A. S. H., and Borrmann, S.: Aerosol quantification with the Aerodyne
Aerosol Mass Spectrometer: detection limits and ionizer background effects, Atmospheric Measurement Techniques, 2, 33–
46, https://doi.org/10.5194/amt-2-33-2009, 2009.

Gong, X., Zhang, J., Croft, B., Yang, X., Frey, M. M., Bergner, N., Chang, R. Y.-W., Creamean, J. M., Kuang, C., Martin, R.
V., Ranjithkumar, A., Sedlacek, A. J., Uin, J., Willmes, S., Zawadowicz, M. A., Pierce, J. R., Shupe, M. D., Schmale, J., and
Wang, J.: Arctic warming by abundant fine sea salt aerosols from blowing snow, Nat. Geosci., 16, 768–774,
https://doi.org/10.1038/s41561-023-01254-8, 2023.

Pisso, I., Sollum, E., Grythe, H., Kristiansen, N. I., Cassiani, M., Eckhardt, S., Arnold, D., Morton, D., Thompson, R. L., Groot
Zwaaftink, C. D., Evangeliou, N., Sodemann, H., Haimberger, L., Henne, S., Brunner, D., Burkhart, J. F., Fouilloux, A.,
Brioude, J., Philipp, A., Seibert, P., and Stohl, A.: The Lagrangian particle dispersion model FLEXPART version 10.4,
Geoscientific Model Development, 12, 4955–4997, https://doi.org/10.5194/gmd-12-4955-2019, 2019.